Force on a compressible sphere and the resonance of a bubble in standing surface acoustic waves

Shen Liang, Wang Chaohui,* and Hu Qiao
State Key Laboratory of Manufacturing Systems Engineering, Xi'an Jiaotong University, Xi'an, Shaanxi 710049, China
and Shaanxi Key Laboratory of Intelligent Robots, Xi'an Jiaotong University, Xi'an, Shaanxi 710049, China

(Received 3 April 2018; published 23 October 2018)

In this paper, the theory for acoustic radiation force exerted by standing surface acoustic waves (SSAWs) is extended to a compressible sphere in inviscid fluids. The conventional theory, developed in plane standing waves, fails to predict the radiation force incident on particles in the SSAW. Our extended formulas reveal that, in the direction normal to the piezoelectric substrate, the acoustic radiation force cannot only push the sphere away, but also pull it back towards the substrate. In the direction parallel to the substrate, both the magnitude of the radiation force and the equilibrium positions for particles can be actively tuned by changing the Rayleigh angle. This is exceedingly meaningful for particle positioning by tilted angle SSAWs and SSAWs. Furthermore, the Rayleigh angle can also be used to actively regulate the resonance point and peak for bubbles acted on by SSAWs. The extended theory can thus be used in the design of SSAWs for manipulating particles and bubbles.

DOI: 10.1103/PhysRevE.98.043108

I. INTRODUCTION

Microfluidics has emerged as an excellent platform for biochemistry detection [1,2] and pharmaceutical engineering [3], which has spurred steadily increasing interest and research efforts in the development of new applications. In the research, many new physics applications, including acoustics [4], optics [5], dielectrophoresis [6], etc., are integrated into the microfluidic platform, leading to great improvement in its functionality, versatility, and performance. Among all the developed technologies, acoustophoresis [7,8] stands out due to its label-free, noncontact nature, and great biocompatibility even proved by extensive health monitoring for pregnancy [9]. Particles such as cells [10], funguses [11], and organisms suspended in an acoustophoresis system are primarily set in motion by two types of forces [12]: the acoustic radiation force and the drag force stemming from acoustic streaming.

Acoustic radiation force acting on a particle suspended in fluids is a time-averaged second-order force arising from the scattering of the incident waves. To a certain extent, the force is similar to the optical radiation force exerted by the electromagnetic wave on an electrically or magnetically responsive target [13]. Theoretical analysis of acoustic radiation force provides a more profound understanding of acoustophoresis, and thereby assists in more refined microfluidic applications.

The original theory of acoustic radiation force could date back to King [14], who first theoretically calculated the force due to a plane wave incident on a rigid particle freely suspended in nonviscous fluids. The primary formula, unfortunately limited to particles with large acoustic impedance, was extended by Yosioka and Kawasima [15] to take into account the compressibility of the sphere, such that the motion of a liquid droplet or even a gas bubble could be predicted. In 1962, the generalization of the theory for acoustic radiation force was done by Gorkov [16], but still limited to the ideal host medium and the long-wavelength limit. After that, Hasegawa [17–20] theoretically and experimentally investigated the influences of both the elasticity of spheres and the absorption of sound waves in particle material on the radiation force. Wei and Marston [21–25] developed general theoretical schemes for calculating the force exerted on cylindrical objects and carried out experiments to verify the schemes. Danilov and Mironov [26], Doinikov [27,28], Settnes and Bruus [29], and Karlsen and Bruus [30] further developed the theory of acoustic radiation force by considering the viscosity [31] and thermoviscosity of the host medium. In addition, the radiation forces caused by different types of sound waves such as cylindrical waves [32,33], spherical waves [34], Bessel beams [35], Gaussian beams [36], and Bessel vortex beams [37] were all analyzed. However, to the best of our knowledge, the acoustic radiation force exerted by standing surface acoustic waves (SSAWs) [38] gains much less attention in the research.

We have in the past theoretically investigated the radiation force due to SSAWs on cylindrical structures [39,40]. Actually, spherical objects are more popular in microfluidics. This urges us to extend our previous theory to spherical particles, which will be extremely meaningful for particle manipulations using SSAWs such as positioning particles [41–47], patterning cells [38,48,49], and handling droplets [50,51]. In this work, we develop the theory of acoustic radiation force exerted by the SSAW on a compressible sphere in nonviscous fluids by accounting for the dependence on Rayleigh angle. Our expressions can be used to calculate the radiation force on droplets, bubbles, and solid particles in the SSAW-based microfluidics. In addition, they can also be used to calculate acoustic radiation force exerted by two plane traveling waves with the same amplitude and frequency. More importantly, they are applicable to microsized particles and

*chhw@mail.xjtu.edu.cn

may lose accuracy in calculating nanosized particles, because the inviscid fluid assumption is invalid.

The radiation force caused by a traveling wave is normally directed away from the transducer, resulting in a great restriction for traveling waves in particle positioning. Traditionally, a desirable acoustic tweezer is able to either attract or repel a particle. This is realized by a pair of transducers generating counterpropagating sound beams [52]. However, Marston [35] theoretically broke the limitation for traveling waves in particle manipulations, since he predicted the ability of two-direction driving for a single Bessel beam. In this paper, the radiation force exerted by SSAWs is predicted to attract or push away the particle. Additionally, in the direction parallel to the substrate, the classical radiation force F_{PSW} derived in plane standing waves (PSWs) is almost used in all the SSAW-based particle manipulations [38,49,50,53–59], which is expressed by

$$F_{\mathrm{PSW}} = -\frac{k_f {P_f}^2 V_p \kappa_f}{4}\left(\frac{5\rho_p - 2\rho_f}{2\rho_p + \rho_f} - \frac{\kappa_p}{\kappa_f}\right)\sin(2k_f x), \quad (1)$$

where k_f, P_f, V_p, κ_p, κ_f, ρ_p, ρ_f, and x are wave number, pressure amplitude, particle volume, compressibility of the particle, compressibility of the fluid, density of the particle, density of the fluid, and distance from the particle to a pressure node, respectively. In this paper, our expression shows that the Rayleigh angle has profound influences on the radiation force, leading to a different prediction for the gathering places of particles. This means that a particle, expected to be focused at pressure nodes according to Eq. (1), may be collected at pressure antinodes based on our formula.

When a gas bubble with extremely low density is incident by sound waves, the resonance occurs only for special size parameters $(k_f a)$ [15,60–62], where a is the radius of the bubble. While a bubble is acted on by the SSAW, both the resonance point and peak show great dependence on the Rayleigh angle. Thus, we provide approximate expressions to evaluate the radiation force exerted on a bubble in the long-wavelength limit, and further estimate both the resonance point and peak to assist in bubble manipulations.

II. EVALUATING THE SCATTERING COEFFICIENTS

The SSAW is formed by two traveling surface acoustic waves (TSAWs) generated by a pair of interdigital transducers (IDTs), which are fabricated on a piezoelectric substrate, as depicted in Fig. 1(a). When traveling along the substrate-fluid boundary, each TSAW with negligible attenuation can be regarded as a plane progressive wave incident along Rayleigh angle β [63] with respect to the orthogonal. The angle is determined by the phase velocity of TSAWs c_s and sound speed in fluids c_f,

$$\beta = \arcsin(c_f/c_s). \quad (2)$$

A spherical coordinate system (r, θ, φ) is built at the instantaneous center of the compressible sphere with radius a, as sketched in Fig. 1(b). The incident SSAW ϕ_c can thus be expressed by

$$\phi_c = \phi_0 e^{i\mathbf{k_1}\cdot(\mathbf{y_0}+\mathbf{r})-iwt} + \phi_0 e^{i\mathbf{k_2}\cdot(\mathbf{y_0}+\mathbf{r})-iwt}, \quad (3)$$

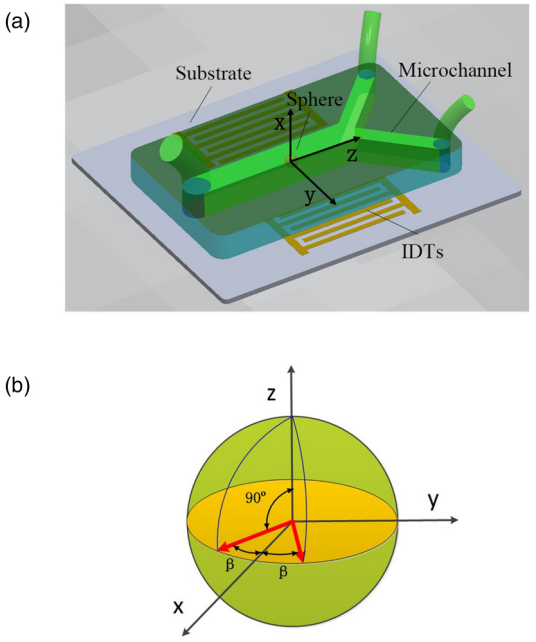

FIG. 1. (a) Two TSAWs generated by a pair of IDTs propagate towards each other. Additionally, the positive x direction in the global Cartesian coordinate system is normal to the piezoelectric substrate, while the positive y direction is parallel to the substrate. (b) A local spherical coordinate system (r, θ, φ) is built at the instantaneous center of the sphere.

where ϕ_0 is the amplitude, $\mathbf{k_1}$ and $\mathbf{k_2}$ are wave vectors of the two TSAWs, ω is the angular frequency, $\mathbf{y_0}$ is a vector pointing from a pressure node to the center of the suspended sphere, and $\mathbf{r}$ is the location vector. According to the identity Eq. (A1) in the appendix, the SSAW can be expanded in a spherical partial-wave series with respect to the spherical coordinate system as

$$\begin{aligned}
\phi_c &= \phi_0 e^{-i\omega t}(e^{i\mathbf{k_1}\cdot(\mathbf{y_0}+\mathbf{r})} + e^{i\mathbf{k_2}\cdot(\mathbf{y_0}+\mathbf{r})}) \\
&= \phi_0 e^{-i\omega t}(e^{ik_f y_0 \sin\beta} e^{ik_f r\cos\gamma_1} + e^{-ik_f y_0 \sin\beta} e^{ik_f r\cos\gamma_2}) \\
&= \phi_0 \sum_{(n=0)}^{\infty} i^n (2n+1) j_n(k_f r)\Big[2P_n(0)P_n(\cos\theta) \\
&\quad \times \cos(k_f y_0 \sin\beta) + 2\sum_{(m=1)}^{n}\frac{(n-m)!}{(n+m)!}P_n^m(0)P_n^m(\cos\theta) \\
&\quad \times (2\cos(k_f y_0 \sin\beta)\cos m\varphi \cos m\beta \\
&\quad + i2\sin(k_f y_0 \sin\beta)\sin m\varphi \sin m\beta)\Big] e^{-i\omega t}, \quad (4)
\end{aligned}$$

where k_f is the wave number of the two TSAWs, γ_1 and γ_2 are the angles between the position vector $\mathbf{r}$ and wave vectors of the two TSAWs (i.e., $\mathbf{k_1}$ and $\mathbf{k_2}$), respectively, $j_n(k_f r)$ is the first kind of spherical Bessel function of order n, and $P_n^m(\cos\theta)$ is introduced to denote associated Legendre polynomial.

When illustrated by the incident wave, the suspended sphere generates a scattered wave,

$$\phi_s = \phi_0 \sum_{(n=0)}^{\infty} i^n (2n+1) s_n h_n(k_f r) \Bigg[2P_n(0)P_n(\cos\theta) \times \cos(k_f y_0 \sin\beta) + 2 \sum_{(m=1)}^{n} \frac{(n-m)!}{(n+m)!} P_n^m(0) P_n^m(\cos\theta) \times (2\cos(k_f y_0 \sin\beta)\cos m\varphi \cos m\beta + i2\sin(k_f y_0 \sin\beta)\sin m\varphi \sin m\beta) \Bigg] e^{-i\omega t}, \quad (5)$$

where $h_n(k_f r)$ denotes the first kind of spherical Hankel function of order n, and s_n is the scattering coefficient, which is determined by the boundary conditions at the surface of the sphere.

The total wave ϕ_f, transporting in fluids, consists of both the incident SSAW and the scattered wave, such that

$$\phi_f = \phi_c + \phi_s. \quad (6)$$

When the scattering occurs, a longitudinal wave ϕ_p is produced in the particle,

$$\phi_p = \phi_0 \sum_{(n=0)}^{\infty} i^n (2n+1) a_n j_n(k_p r) \Bigg[2P_n(0)P_n(\cos\theta) \times \cos(k_f y_0 \sin\beta) + 2 \sum_{(m=1)}^{n} \frac{(n-m)!}{(n+m)!} P_n^m(0) P_n^m(\cos\theta) \times (2\cos(k_f y_0 \sin\beta)\cos m\varphi \cos m\beta + i2\sin(k_f y_0 \sin\beta)\sin m\varphi \sin m\beta) \Bigg] e^{-i\omega t}, \quad (7)$$

where k_p is the wave number in the compressible sphere, and a_n is an unknown coefficient describing a certain longitudinal wave.

In practical viscous fluids, great tangential velocity gradient occurs on the viscous boundary, based on which the transverse stress and velocity are continuous. Since the viscous boundary is very thin for the SSAW-based microfluidics, it has little influence on the sound field. Therefore, the fluid is assumed to be inviscid, and the continuities of the transverse stress and velocity on the boundary are invalid. As a result, the boundary conditions are the continuities of both normal velocity and normal stress on the surface of the submerged sphere,

$$u_{fr}|_{r=a} = u_{pr}|_{r=a}, \quad (8a)$$

$$\sigma_{rr}^{f}|_{r=a} = \sigma_{rr}^{p}|_{r=a}, \quad (8b)$$

where u_{fr} and u_{pr} are the normal velocities in the host medium and the sphere, respectively, σ_{rr}^{f} and σ_{rr}^{p} are the normal stresses in the host medium and the suspended particle, respectively, The four quantities can all be expressed by the velocity potentials,

$$\sigma_{rr}^{f} = -i\omega\rho_f \phi_f, \quad (9a)$$

$$\sigma_{rr}^{p} = -i\omega\rho_p \phi_p, \quad (9b)$$

$$u_{fr} = \frac{\partial \phi_f}{\partial r}, \quad (9c)$$

$$u_{pr} = \frac{\partial \phi_p}{\partial r}. \quad (9d)$$

Substituting Eq. (9) into Eq. (8) and combining Eq. (6), two equations with two unknowns are obtained:

$$\rho_p a_n j_n(x_p) = \rho_f (j_n(x_f) + s_n h_n(x_f)), \quad (10a)$$

$$a_n j_n'(x_p) x_p = j_n'(x_f) x_f + s_n h_n'(x_f) x_f, \quad (10b)$$

where $x_f = k_f a$ and $x_p = k_p a$ are dimensionless size factors. Consequently, the scattering coefficient is written as

$$s_n = \frac{\begin{bmatrix} \overline{\rho} j_n(x_p) & j_n(x_f) \\ j_n'(x_p)x_p & j_n'(x_f)x_f \end{bmatrix}}{\begin{bmatrix} \overline{\rho} j_n(x_p) & -h_n(x_f) \\ j_n'(x_p)x_p & -h_n'(x_f)x_f \end{bmatrix}}, \quad (11)$$

where $\overline{\rho} = \rho_p/\rho_f$ is the relative density. Once the scattering coefficient is obtained, the total velocity potential in the host medium can be calculated.

III. ACOUSTIC RADIATION FORCE IN THE *x* DIRECTION

In inviscid fluids, acoustic radiation force $\mathbf{F}$ can be derived by integrating the time-average radiation-stress tensor $\langle \mathbf{\Pi} \rangle$ on the sphere surface according to Ref. [15]. Thus,

$$\mathbf{F} = -\oint_s \langle \mathbf{\Pi} \rangle d\mathbf{s} = -\oint_s \langle \mathbf{p_2} + \rho_f \mathbf{u_1}\mathbf{u_1} \rangle d\mathbf{s}, \quad (12)$$

where s is the area on the surface of the sphere, $\langle \mathbf{p_2} \rangle$ is a scalar matrix with element $\langle p_2 \rangle$ [39], and $\mathbf{u_1}$ is the first-order velocity in the host medium. The radiation force can thus be expressed by

$$\mathbf{F} = -\iint_s \Bigg[\left(\frac{1}{2}\frac{\rho_f}{{c_f}^2} \left\langle \left(\mathrm{Re}\left[\frac{\partial \phi_f}{\partial t} \right] \right)^2 \right\rangle - \frac{1}{2}\rho_f \langle |\nabla \mathrm{Re}[\phi_f]|^2 \rangle \right) \times \mathbf{n} + \rho_f \langle (u_n \mathbf{n} + u_t \mathbf{t}) u_n \rangle \Bigg] ds, \quad (13)$$

where $u_n\mathbf{n}$ and $u_t\mathbf{t}$ are the velocities in the normal and tangential directions, respectively.

The radiation force exerted by the SSAW is decomposed into two forces F_x and F_y, pointing to the x and y directions, respectively. First, according to Eq. (13), we have

$$F_x = F_{xnn} + F_{xtt} + F_{xnt} + F_{xt} \quad (14)$$

where each term is given as

$$F_{xnn} = -\frac{1}{2}\rho_f a^2 \int_0^{\pi}\int_0^{2\pi} \langle {u_{fr}}^2 \rangle|_{r=a} \sin^2\theta \cos\varphi d\varphi d\theta, \quad (15a)$$

$$F_{xtt} = \frac{1}{2}\rho_f a^2 \int_0^{\pi}\int_0^{2\pi} \langle {u_{f\theta}}^2 + {u_{f\varphi}}^2 \rangle|_{r=a} \sin^2\theta \times \cos\varphi d\varphi d\theta, \quad (15b)$$

$$F_{xnt} = -\rho_f a^2 \int_0^{\pi}\int_0^{2\pi} (\langle u_{fr} u_{f\theta} \rangle \cos\theta \cos\varphi - \langle u_{fr} u_{f\varphi} \rangle \sin\varphi)|_{r=a} \sin\theta d\varphi d\theta, \quad (15c)$$

$$F_{xt} = -\frac{\rho_f}{2{c_f}^2}a^2\int_0^{\pi}\int_0^{2\pi}\left\langle \mathrm{Re}\left[\frac{\partial\phi_f}{\partial t}\right]^2\right\rangle\Big|_{r=a}\sin^2\theta \times \cos\varphi d\varphi d\theta, \tag{15d}$$

where $u_{f\theta}$ and $u_{f\varphi}$ are the components of velocity in fluids, pointing to the polar and azimuthal directions, respectively.

Furthermore, the radiation force is usually characterized by a dimensionless factor Y_{px}, which can be written as

$$Y_{px} = F_x/(S_c E), \tag{16}$$

where $S_c = \pi a^2$ is the cross-sectional area of the immersed sphere, and $E = \frac{1}{2}\rho_f {k_f}^2 {\phi_0}^2$ represents the characteristic energy density of the incident wave. The real and imaginary parts of the scattering coefficient (i.e., α_n and β_n, respectively) are introduced to simplify the expression for Y_{px}. Substituting Eq. (14) into Eq. (16) and using Eqs. (A2)–(A4), we obtain a simple and valuable expression for Y_{px},

$$Y_{px} = -\frac{16}{{x_f}^2}\sum_{(n=0)}^{\infty}(\alpha_n + \alpha_{n+1} + 2\alpha_n\alpha_{n+1} + 2\beta_{n+1}\beta_n)D_n, \tag{17}$$

where

$$D_n = \sum_{(m=0)}^{n}\left[\frac{(n-m+1)!}{(n+m+1)!}P_n^{m+1}(0)P_{n+1}^{m}(0) - \frac{(n-m)!}{(n+m)!} \times P_n^m(0)P_{n+1}^{m+1}(0)\right](\cos^2(k_f y_0\sin\beta)\cos(m+1) \times \beta\cos m\beta + \sin^2(k_f y_0\sin\beta)\sin(m+1)\beta\sin m\beta). \tag{18}$$

Following the procedure in Ref. [39], the exact solution for Y_{px} is examined by considering two special Rayleigh angles (0° and 90°). When $\beta = 0°$, the SSAW degenerates into a plane traveling wave (PTW) transporting in the positive x direction. Our expression reduces to what Hasegawa obtained in PTWs [19]. When $\beta = 90°$, the SSAW degenerates into a PSW in the y direction. Substituting $\beta = 90°$ into Eq. (17), the value of Y_{px} equals zero, which is consistent with the prediction according to the symmetry principle.

In the design of SSAW-based devices, the exact solution for Y_{px} is applicable to a sphere with any radius, but it includes infinite terms resulting in a trouble for researchers in the calculation. Additionally, the radiuses of particles for many applications in microfluidics fall in the range of $a \ll \lambda_f$ (i.e., $x_f \ll 1$). Thus, Taylor expansion and truncation can be applied to simplify Y_{px}, yielding an approximate formula to assist in the calculation:

$$Y_{apx} = \frac{8{x_f}^4}{9}\left[\frac{2\kappa_p(\overline{\rho}-1)}{\kappa_f\overline{\rho}} - \frac{3(\overline{\rho}-1)^2}{(2\overline{\rho}+1)^2} + \frac{4\kappa_p(\overline{\rho}-1)}{\kappa_f(2\overline{\rho}+1)} - \frac{4(\overline{\rho}-1)}{(2\overline{\rho}+1)}\right]\cos^2(k_f y_0\sin\beta)\cos\beta - \frac{8{x_f}^4(\overline{\rho}-1)^2}{3(2\overline{\rho}+1)^2}[\cos^2(k_f y_0\sin\beta)\cos\beta\cos 2\beta + \sin^2(k_f y_0\sin\beta)\sin\beta\sin 2\beta]. \tag{19}$$

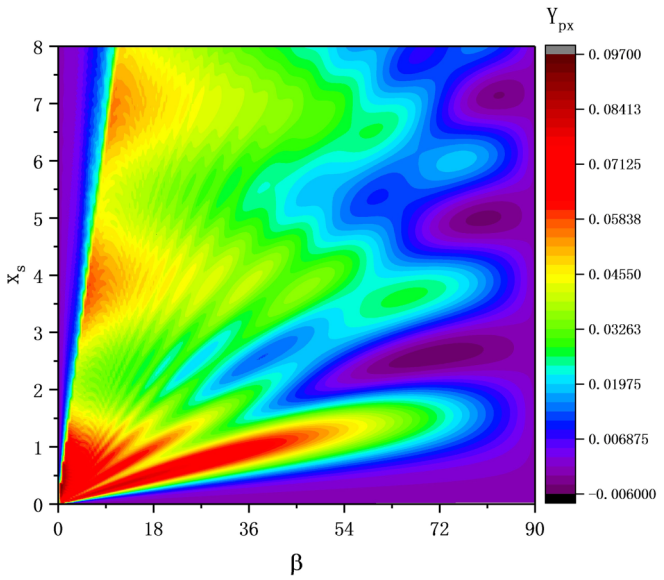

FIG. 2. The value of Y_{px} from Eq. (17) is plotted in the bandwidths $0 \leqslant x_s \leqslant 8$ and $0° \leqslant \beta \leqslant 90°$ using the parameters from the case of an oil sphere ($\rho_p = 922.6$ kg/m^3, $c_p = 1445$ m/s) located at pressure antinodes and immersed in water ($\rho_f = 996.6$ kg/m^3, $c_f = 1502$ m/s).

Special attention should be drawn to the fact that the approximate formula cannot be used to evaluate the radiation force exerted on spherical bubbles, because the relative density $\overline{\rho}$ is assumed to be far larger than x_f in the simplification, which is not valid for bubbles. The approximate formula for the radiation force exerted on bubbles is analyzed in the next part. Numerical calculations are carried out to illustrate the Rayleigh angle effects on acoustic radiation force by using a MATLAB code. Following the method in Ref. [39], we introduce the wave number $k_s = k_f\sin\beta$, the wavelength λ_s, and the size factor $x_s = k_s a$ to make the calculations more suitable for practical microfluidic applications. These parameters (k_s, λ_s, and x_s) are usually used to characterize the SSAW-based microfluidics. In addition, the wavelength of the SSAW on the substrate is set to $\lambda_s = 0.4$ mm in the following numerical analysis.

From the mathematical point of view, the dimensionless factor Y_{px} is found to show a periodic change as a result of the position-dependent terms $\cos^2(k_f y_0\sin\beta)$ and $\sin^2(k_f y_0\sin\beta)$ in D_n. Thus, both the maximum and minimum values of Y_{px} are predicted to reach, when the suspended particles are located at pressure antinodes or nodes (i.e., for example, $y_0 = 0$ or $y_0 = \lambda_s/4$, respectively). The numerical computations of the dimensionless factor Y_{px} are shown using the parameters from the case of an oil particle ($\rho_p = 922.6$ kg/m^3, $c_p = 1445$ m/s) suspended in water ($\rho_f = 996.6$ kg/m^3, $c_f = 1502$ m/s) in Figs. 2 and 3, where the values of y_0 are set to 0 mm and 0.1 mm, respectively. In each figure, the two-dimensional plots are evaluated in the bandwidths $0 \leqslant x_s \leqslant 8$ and $0° \leqslant \beta \leqslant 90°$. Inspection of Figs. 2 and 3 reveals that the values of Y_{px} exhibit great dependence on the Rayleigh angle for x_s in the whole tested range from 0 to 8. Additionally, for most values of the two considered parameters (i.e., size factor and Rayleigh angle),

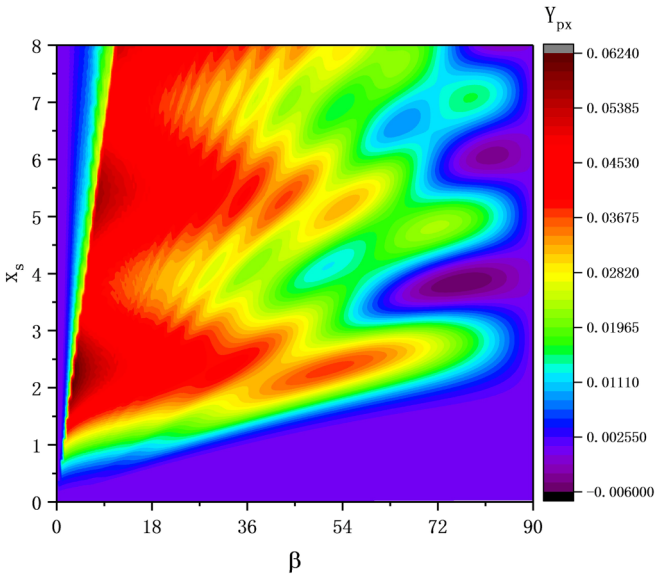

FIG. 3. The value of Y_{px} from Eq. (17) is plotted in the bandwidths $0 \leqslant x_s \leqslant 8$ and $0^\circ \leqslant \beta \leqslant 90^\circ$ using the parameters from the case of an oil sphere located at pressure nodes and immersed in water.

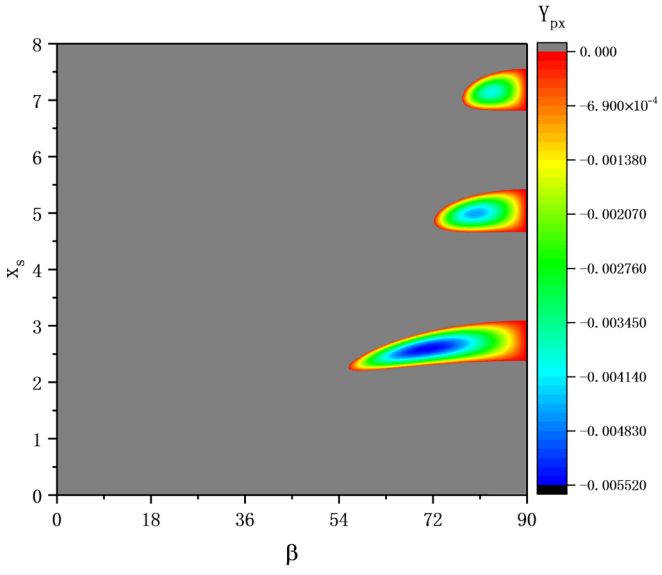

FIG. 4. The negative value of Y_{px} is clearly depicted in the bandwidths $0 \leqslant x_s \leqslant 8$ and $0^\circ \leqslant \beta \leqslant 90^\circ$ by setting all the positive value to zero and using the parameters from the case of an oil sphere located at pressure antinodes and immersed in water.

the sign of the corresponding Y_{px} is positive, which means the oil sphere is predicted to be pushed away from the piezoelectric substrate. Furthermore, with the increase of the Rayleigh angle, the magnitude of Y_{px} exhibits a decreasing trend, and even reverses its sign when the Rayleigh angle approaches 90°.

Note that the inviscid fluid assumption is also valid in the case of an oil sphere ($\rho_p = 922.6$ kg/m^3, $\eta_p = 4.153 \times 10^{-2}$Pa s) immersed in water. The IDTs are assumed to be fabricated on the most popular piezoelectric substrate LiNbO^3 ($c_s = 3994$ m/s) and with wavelength $\lambda_s = 0.4$ mm. The viscous boundary layer is $\delta = \sqrt{\nu/\omega} = 0.85$ μm, which is very small and has little influence on acoustic radiation force for microsized particles.

We further search and clearly depict the negative value of the acoustic radiation force incident on an oil sphere submersed in water by setting the positive value of Y_{px} to zero in Figs. 4 and 5, where the values of y_0 are 0 mm and 0.1 mm, respectively. In addition, the radiation force is evaluated in the area $0 \leqslant x_s \leqslant 8$ and $0^\circ \leqslant \beta \leqslant 90^\circ$. Inspection of Eq. (17) reveals that the value of Y_{px} for any given size factor and Rayleigh angle falls in a certain range, in which the minimum and maximum values are obtained by substituting $y_0 = 0$ mm and $y_0 = 0.1$ mm into Eq. (17). Visual comparison of Figs. 4 and 5 shows that there is no overlapping area for the negative "island" of Y_{px}, which means the radiation force exerted by the SSAW cannot be all negative for different values of y_0. Thus, the attractive and repulsive behaviors of the SSAW may occur alternately for the considered parameters, when varying the position quantity y_0.

The curve for Y_{px} evolving with size factor x_s is very common in the study of acoustic radiation force. In Fig. 6, the value of Y_{px} is plotted in the range $0 \leqslant x_s \leqslant 8$ using the parameters from the case of an oil sphere located at pressure antinodes and immersed in water. Obviously, curves are totally different for the four Rayleigh angles. The value of Y_x overall drops down with the increase of the Rayleigh angle. Furthermore, when the Rayleigh angle is 80°, Y_x can be negative for particles with certain sizes. Thus, the SSAW-based microfluidics can be used to attract particles in the height direction.

The negative behavior is also observed in the case of spherical particles illuminated by a Bessel beam, for which the phenomenon is caused by the suppression of the backscattering [35]. We find that the explanation also holds for the attractive behavior of the SSAW. The time- and amplitude-independent

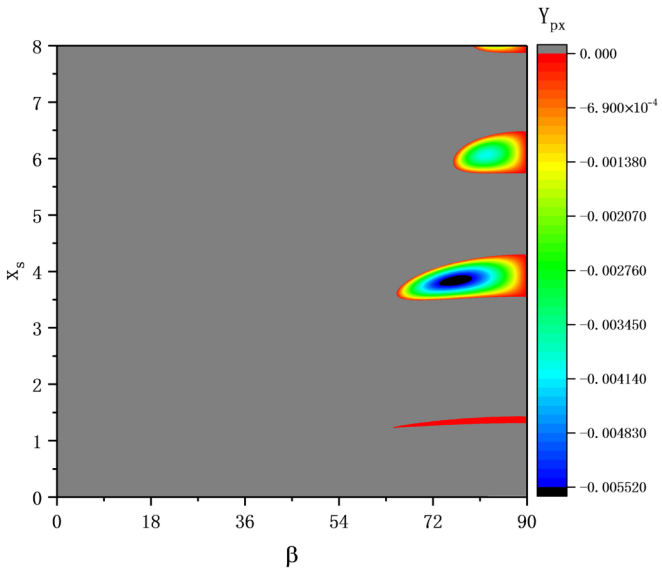

FIG. 5. The negative value of Y_{px} is clearly depicted in the bandwidths $0 \leqslant x_s \leqslant 8$ and $0^\circ \leqslant \beta \leqslant 90^\circ$ by setting all the positive value to zero and using the parameters from the case of an oil sphere located at pressure nodes and immersed in water.

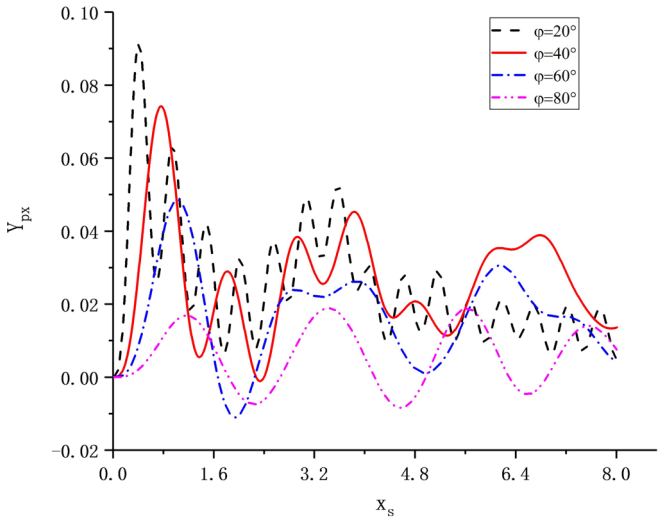

FIG. 6. The value of Y_{px} from Eq. (17) is plotted in the range $0 \leqslant x_s \leqslant 8$ using the parameters from the case of an oil sphere located at pressure antinodes and immersed in water. In addition, four different Rayleigh angles (20°, 40°, 60°, and 80°) are considered in the figure.

form of the scattering potential magnitude $|\phi_s/(\phi_0 e^{-i\omega t})|$ with polar angle being 90° is plotted by varying the azimuthal angle in Fig. 7, where both the attractive and repulsive cases are considered with the parameters (x_s, β, y_0) being $(2.5, 72^\circ, 0)$ and $(1, 72^\circ, 0)$, respectively. Obviously, lower values of $|\phi_s/(\phi_0 e^{-i\omega t})|$ for $(2.5, 72^\circ, 0)$ are found in the vicinity of $\varphi = 180^0$, which supports the argument that the attractive behavior is due to the suppression of the scattering into the backward hemisphere. While for the repulsive case, the scattering into the forward hemisphere is suppressed, since

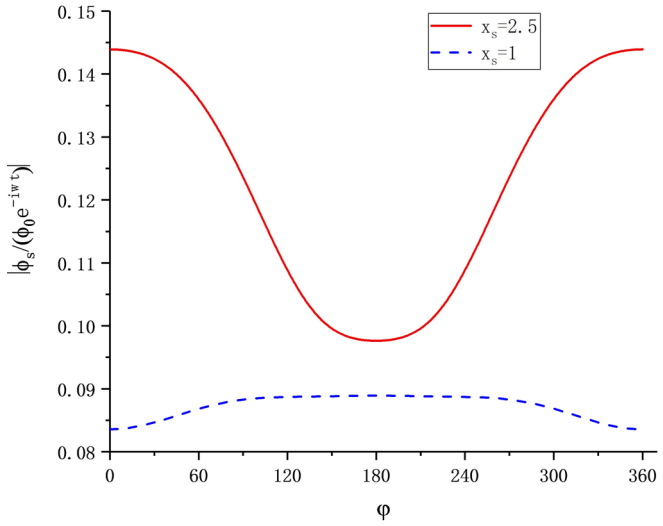

FIG. 7. The time- and amplitude- independent form of the scattering potential $|\phi_s/(\phi_0 e^{-i\omega t})|$ is plotted by varying the azimuthal angle and fixing the polar angle $\theta = 90^\circ$. In the figure, the scattered potential for both the attractive and repulsive behavior are analyzed with the parameters (x_s, β, y_0) being $(2.5, 72^\circ, 0)$ and $(1, 72^\circ, 0)$, respectively. In addition, parameters used in the figure are from the case of water medium with a suspended oil sphere.

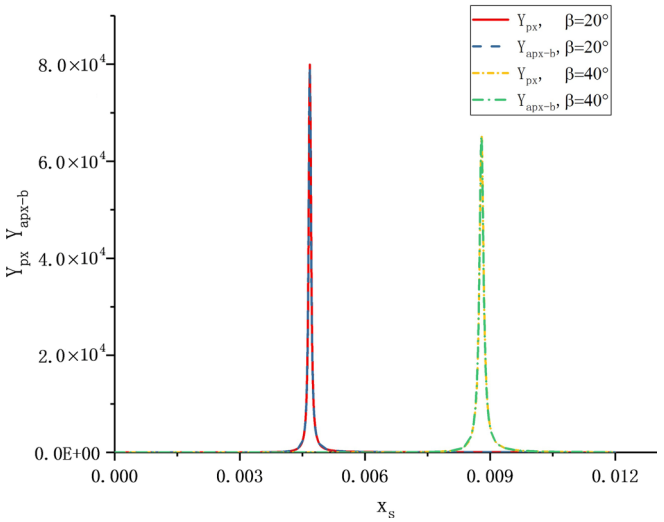

FIG. 8. Both the exact and approximate expressions for the radiation force function in the x direction (i.e., Y_{px} and Y_{apx-b}, respectively) are plotted by varying the size factor x_s using the parameters from the case of an air sphere ($\rho_p = 1.161$ kg/m^3, $c_p = 347.4$ m/s) immersed in water ($\rho_f = 996.6$ kg/m^3, $c_f = 1502$ m/s). In addition, two different Rayleigh angles (i.e., 20° and 40°) are considered in the numerical calculations.

lower values of $|\phi_s/(\phi_0 e^{-i\omega t})|$ are observed in the vicinity of $\varphi = 0^0$.

The resonance of bubbles in the x direction

Theoretical analysis of the resonance of bubbles caused by the SSAW is extremely meaningful for manipulating them [64] and inducing acoustic streaming [65]. Following the method used by Lee and Wang [62], we allow the possibility that $\overline{\rho}$ can be comparable with ${x_f}^2$ and simplify the dimensionless factor Y_{px} using Taylor expansion and truncation, such that

$$Y_{apx-b} = \frac{16}{\left(\frac{x_s}{\sin\beta}\right)^2 + \left(\frac{3\kappa_f \sin^2\beta}{\kappa_p {x_s}^2} - 1\right)^2} \cos^2(k_s y_0)\cos\beta. \quad (20)$$

When $3\kappa_f \sin^2\beta/(\kappa_p {x_s}^2) - 1 = 0$, the motion corresponds to the monopole oscillation resonance of bubbles. The resonance point $x_{sx-\text{peak}}$ can thus be evaluated by

$$x_{sx-\text{peak}} = \sqrt{3\frac{\kappa_f}{\kappa_p}}\sin\beta. \quad (21)$$

Substituting Eq. (21) into Eq. (20), the magnitude of the resonance peak $Y_{apx-\text{peak}}$ is obtained:

$$Y_{apx-\text{peak}} = \frac{16\kappa_p \cos\beta}{3\kappa_f}\cos^2(k_s y_0). \quad (22)$$

In Fig. 8, the values of the radiation force functions (i.e.,Y_{px} and Y_{apx-b}) are estimated by considering the case of an air sphere ($\rho_p = 1.161$ kg/m^3, $c_p = 347.4$ m/s) immersed in water ($\rho_f = 996.6$ kg/m^3, $c_f = 1502$ m/s). Comparison of the values calculated based on the exact and approximate solutions for two different Rayleigh angles (i.e., $\beta = 20^\circ$ and 40°) reveals high accuracy of the expression Y_{apx-b}. In Fig. 9,

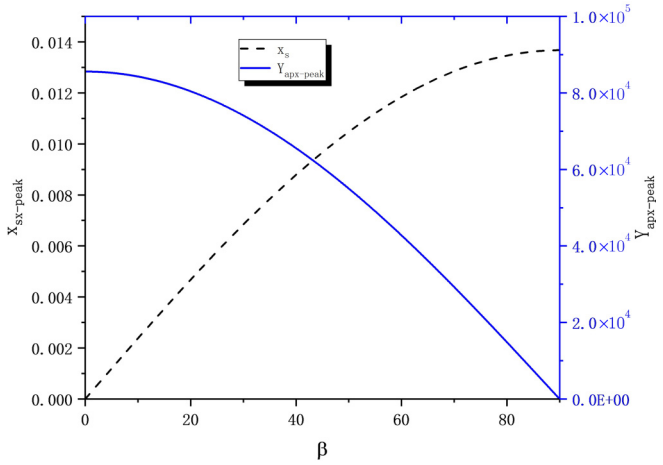

FIG. 9. The approximate expressions for the resonance point and peak in the x direction (i.e., Eqs. (21) and (22), respectively) are plotted by varying the Rayleigh angle using the the parameters from the case of an air sphere immersed in water.

both the resonance point and peak are plotted by varying the Rayleigh angle using the same parameters considered in Fig. 8. It is clear that both the resonance point and peak exhibit great dependence on the Rayleigh angle. Furthermore, as the angle increases, so does the resonance point, but the peak value drops. Therefore, the Rayleigh angle can be used to actively tune the resonance of bubbles in the SSAW.

IV. ACOUSTIC RADIATION FORCE IN THE y DIRECTION

Similarly, the radiation force in the y direction (F_y) also consists of four terms,

$$F_{\mathrm{y}} = F_{ynn} + F_{ytt} + F_{ynt} + F_{yt}, \tag{23}$$

where each term is expressed by

$$F_{ynn} = -\frac{1}{2}\rho_f a^2 \int_0^{\pi}\int_0^{2\pi} \langle {u_{fr}}^2\rangle|_{r=a} \sin^2\theta \sin\varphi d\varphi d\theta, \tag{24a}$$

$$F_{ytt} = \frac{1}{2}\rho_f a^2 \int_0^{\pi}\int_0^{2\pi} \langle {u_{f\theta}}^2 + {u_{f\varphi}}^2\rangle|_{r=a} \sin^2\theta \sin\varphi d\varphi d\theta, \tag{24b}$$

$$F_{ynt} = -\rho_f a^2 \int_0^{\pi}\int_0^{2\pi} (\langle u_{fr}u_{f\theta}\rangle \cos\theta \sin\varphi + \langle u_{fr}u_{f\varphi}\rangle \cos\varphi)|_{r=a} \sin\theta d\varphi d\theta, \tag{24c}$$

$$F_{yt} = -\frac{\rho_f}{2{c_f}^2} a^2 \int_0^{\pi}\int_0^{2\pi} \left\langle \mathrm{Re}\left[\frac{\partial\phi}{\partial t}\right]^2\right\rangle\Bigg|_{r=a} \sin^2\theta \sin\varphi d\varphi d\theta. \tag{24d}$$

Substituting Eq. (24) into Eq. (23) and noting $F_y = Y_{py} S_c E$, the radiation force function in the y direction is obtained. The real and imaginary parts (i.e., α_n and β_n, respectively) of the scattering coefficient s_n are employed to simplify the expression for Y_{py}, such that

$$Y_{py} = \frac{8}{{x_f}^2} \sum_{(n=0)}^{\infty} (\beta_n - \beta_{n+1} - 2\alpha_n\beta_{n+1} + 2\alpha_{n+1}\beta_n) E_n, \tag{25}$$

where

$$E_n = \sum_{(m=0)}^{n} \sin(2k y_0 \sin\beta) \sin(2m+1)\beta \left[\frac{(n-m)!}{(n+m)!} \times P_n^m(0) P_{n+1}^{m+1}(0) + \frac{(n-m+1)!}{(n+m+1)!} P_n^{m+1}(0) P_{n+1}^m(0)\right]. \tag{26}$$

Two special Rayleigh angles (i.e., 0° and 90°) are considered to examine the expression for Y_{py}. When $\beta = 0°$, the value of Y_{py} equals zero, consistent with the prediction according to the symmetry configuration. When $\beta = 90°$, the SSAW degenerates into a PSW and we recover the formula of the acoustic radiation force function derived in the PSW [Eq. (19) in Ref. [19]].

In the same way, Taylor expansion and truncation are employed to simplify the expression for Y_{py}, resulting in an approximate solution Y_{apy} valid for the case $x_f \ll 1$,

$$Y_{apy} = \frac{8x_f}{3}\left[\left(1 - \frac{\kappa_p}{\kappa_f} + \frac{3}{2}\frac{\overline{\rho}-1}{2\overline{\rho}+1}\right)\sin\beta - \frac{3}{2}\frac{\overline{\rho}-1}{2\overline{\rho}+1}\sin 3\beta\right]\sin(2k y_0 \sin\beta). \tag{27}$$

Note that this expression is not applicable to bubbles. When $\beta = 90°$, the approximate formula is identical to that derived in PSWs [i.e., Eq. (1)]. Inspection of Eq. (27) reveals that the Rayleigh angle can have profound influences on the force, such that researchers may have to take it into account to further improve their designed application devices.

In Fig. 10, the value of the position-independent form of acoustic radiation force function $Y_{py}/\sin(2k_s y_0)$ is plotted in the bandwidths $0 \leqslant x_s \leqslant 8$ and $0° \leqslant \beta \leqslant 90°$ by considering the case of an oil object immersed in water. Inspection of Fig. 10 reveals that the Rayleigh angle plays a dominant role in both the magnitude and direction of acoustic radiation force exerted by the SSAW. In practical applications, the microchannel is configured with a designed angle or parallel to the IDTs, such that the pressure nodal or antinodal lines are crossed with or parallel to the microchannel. For the former case [i.e., tilted angle SSAW (taSSAW) configuration [66]], particles with diverse physical properties deviate from the flow direction with different distances as a consequence of the different radiation force caused by SSAWs. In this configuration, the magnitude of the radiation force is important for particle motion. As shown in Fig. 10, the acoustic radiation force derived in SSAWs can deviate remarkably from that obtained in PSWs (i.e., $\beta = 90°$). Our expression provides a more refined prediction, and thereby has great potential in the design of taSSAWs for particle manipulations.

When the sign of $Y_{py}/\sin(2k_s y_0)$ is positive, the particle in SSAWs experiences a force directed towards pressure nodes. While it is negative, the force is directed towards

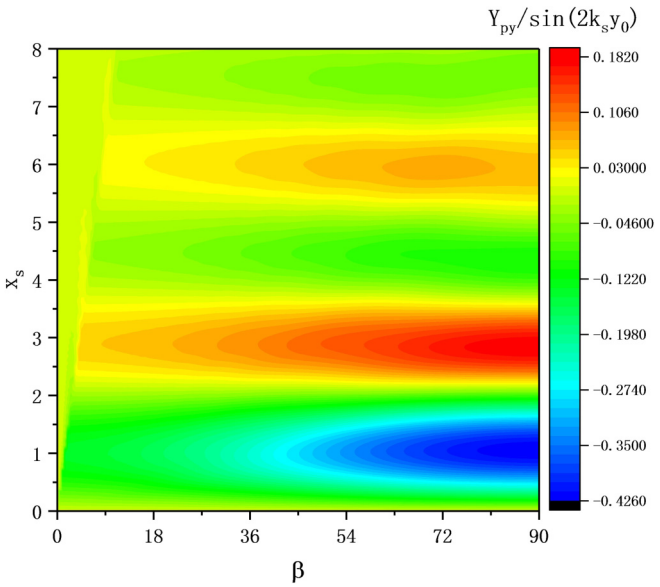

FIG. 10. The value of $Y_{py}/\sin(2k_s y_0)$ based on Eq. (25) is plotted in the bandwidths $0 \leqslant x_s \leqslant 8$ and $0^\circ \leqslant \beta \leqslant 90^\circ$ using the parameters from the case of an oil sphere immersed in water.

pressure antinodes. This is the working mechanism of the SSAW-based microfluidics with parallel configuration. The acoustically soft particles (i.e., the case considered in Fig. 10) are expected to be focused at pressure antinodes according to the theory developed in PSWs, but a different prediction is obtained based on our expression. This means the PSWs theory can provide a wrong prediction in designing SSAWs for particle manipulations. The areas with positive values of $Y_{py}/\sin(2k_s y_0)$ are clearly shown in Fig. 11, which is depicted by setting all the negative values in Fig. 10 to zero. The

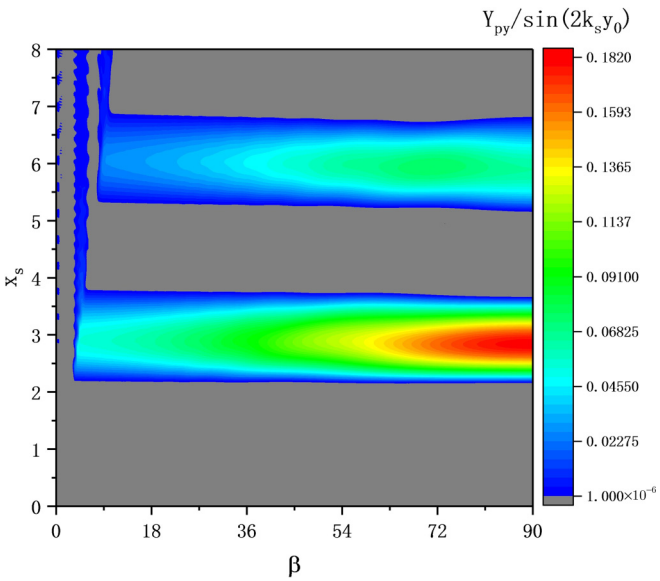

FIG. 11. The positive value of $Y_{py}/\sin(2k_s y_0)$ is clearly depicted in the bandwidths $0 \leqslant x_s \leqslant 8$ and $0^\circ \leqslant \beta \leqslant 90^\circ$ by setting all the negative value to zero and using the parameters from the case of an oil sphere immersed in water.

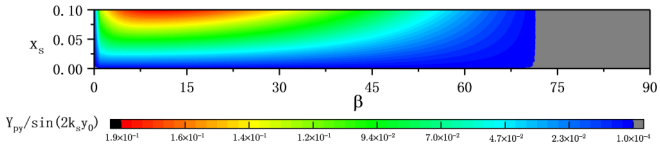

FIG. 12. The positive value of $Y_{py}/\sin(2k_s y_0)$ based on Eq. (25) is plotted in the bandwidths $0 \leqslant x_s \leqslant 0.1$ and $0^\circ \leqslant \beta \leqslant 90^\circ$ by setting all the negative value to zero and using the parameters from the case of a water sphere ($\rho_p = 996.6$ kg/m^3, $c_p = 1502$ m/s) immersed in chloroform medium ($\rho_f = 1487$ kg/m^3, $c_f = 1001$ m/s).

equilibrium positions (i.e., pressure nodes or antinodes) for particles with predetermined sizes can be actively tuned by changing the Rayleigh angle. Note that two different particles can be separated in the parallel configuration, only if they are predicted to be focused at different equilibrium positions. Thus, our expression is exceedingly meaningful for practical applications.

Furthermore, noting that the maximal separation distance is limited to a quarter of the wavelength $\lambda_s/4$, the ability to actively tune equilibrium positions in the longwavelength limit is significant for practical particle separation. In Fig. 12, the value of $Y_{py}/\sin(2k_s y_0)$ for a water droplet ($\rho_p = 996.6$ kg/m^3, $c_p = 1502$ m/s) suspended in chloroform medium ($\rho_f = 1487$ kg/m^3, $c_f = 1001$ m/s) is plotted by varying the Rayleigh angle, and the size factor is limited to $0 \leqslant x_s \leqslant 0.1$. Figure 12 shows that $Y_{py}/\sin(2k_s y_0)$ can change its sign, when the Rayleigh angle is equal to 72°. This reveals that the Rayleigh angle can be used to change equilibrium positions for particles in the long-wavelength limit, and thereby assist in particle handling.

The resonance of bubbles in the y direction

In this part, we also allow the possibility that $\overline{\rho}$ can be comparable with ${x_f}^2$ to simplify the dimensionless factor Y_{py} for bubbles using Taylor expansion and truncation, such that

$$Y_{apy-b} = \frac{-\left(3\kappa_f \sin^2\beta/\kappa_p {x_s}^2 - 1\right)}{\frac{{x_s}^2}{\sin^2\beta} + \left(\frac{3\kappa_f \sin^2\beta}{\kappa_p {x_s}^2} - 1\right)^2} \frac{8}{x_s} \sin^2\beta \sin(2k_s y_0). \tag{28}$$

In Fig. 13, the values of acoustic radiation force functions are evaluated according to both Eqs. (25) and (28) by using the parameters from the case of an air sphere immersed in water. Comparison of the values computed based on the exact and approximate solutions for two different Rayleigh angles (i.e., $\beta = 20^\circ$ and 40°) shows that Y_{apy-b} has great accuracy to capture the value of acoustic radiation force exerted on bubbles. Additionally, inspection of Fig. 12 reveals that the resonance of bubbles occurs in the position very close to the zero point (i.e., $x_s = \sqrt{\frac{3\kappa_f}{\kappa_p}} \sin\beta$). This inspires us to further evaluate the resonance peak. We rewrite Y_{apy-b} as

$$Y_{apy-b} = \frac{-1}{\frac{{x_s}^2/\sin^2\beta}{\left(\frac{3\kappa_f \sin^2\beta}{\kappa_p {x_s}^2} - 1\right)} + \left(\frac{3\kappa_f \sin^2\beta}{\kappa_p {x_s}^2} - 1\right)} \frac{8}{x_s} \sin^2\beta \sin(2k_s y_0). \tag{29}$$

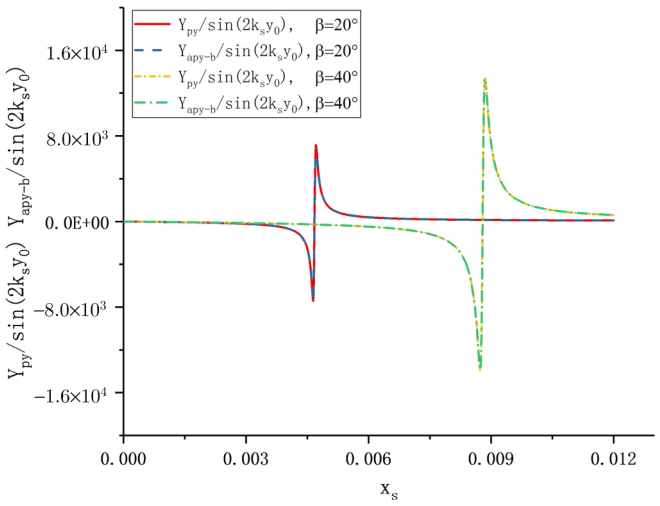

FIG. 13. Both the exact and approximate expressions for the radiation force function in the y direction (i.e., Y_{py} and Y_{apy-b}, respectively) are plotted by varying the size factor x_s using the parameters from the case of an air sphere ($\rho_p = 1.161$ kg/m^3, $c_p = 347.4$ m/s) immersed in water ($\rho_f = 996.6$ kg/m^3, $c_f = 1502$ m/s). In addition, two different Rayleigh angles (i.e., 20° and 40°) are considered in the numerical calculations.

In the vicinity of $x_s = \sqrt{\frac{3\kappa_f}{\kappa_p}}\sin\beta$, only the term $\frac{{x_s}^2/\sin^2\beta}{(3\bar{\rho}{c_p}^2\sin^2\beta/{x_s}^2{c_f}^2-1)}$ is sensitive to the value of x_s. In addition, for $x_s < \sqrt{\frac{3\kappa_f}{\kappa_p}}\sin\beta$,

$$\frac{{x_s}^2/\sin^2\beta}{\left(\frac{3\kappa_f\sin^2\beta}{\kappa_p{x_s}^2}-1\right)}+\left(\frac{3\kappa_f\sin^2\beta}{\kappa_p{x_s}^2}-1\right)\geqslant\frac{2x_s}{\sin\beta}, \tag{30}$$

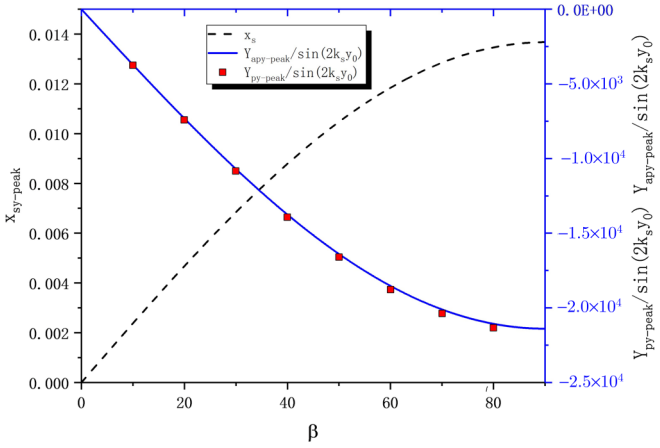

FIG. 14. The approximate expressions for the resonance point and peak in the y direction (i.e., Eq. (21) and Eq. (22), respectively) are plotted by varying the Rayleigh angle using the the parameters from the case of an air sphere immersed in water. Additionally, the exact values of the resonance peak for several Rayleigh angles are also plotted in the figure.

and for $x_s > \sqrt{\frac{3\kappa_f}{\kappa_p}}\sin\beta$,

$$\frac{{x_s}^2/\sin^2\beta}{\left(\frac{3\kappa_f\sin^2\beta}{\kappa_p{x_s}^2}-1\right)}+\left(\frac{3\kappa_f\sin^2\beta}{\kappa_p{x_s}^2}-1\right)\leqslant-\frac{2x_s}{\sin\beta}, \tag{31}$$

such that

$$Y_{apy-\mathrm{peak}}=\pm\frac{4}{{x_s}^2}\sin^3\beta\sin(2k_s y_0). \tag{32}$$

Note that the resonance point is very close to the zero point. Substituting $x_s = \sqrt{\frac{3\kappa_f}{\kappa_p}}\sin\beta$ into Eq. (32), the two resonance peaks can be expressed by

$$Y_{apy-\mathrm{peak}}=\pm\frac{4\sin\beta\kappa_p}{3\kappa_f}\sin(2k_s y_0). \tag{33}$$

Figure 14 shows the approximate values of the resonance point (i.e., $x_{sy} = \sqrt{\frac{3\kappa_f}{\kappa_p}}\sin\beta$) and the first resonance peak [i.e., $Y_{apy-\mathrm{peak}} = -\frac{4\sin\beta\kappa_p}{3\kappa_f}\sin(2k_s y_0)$] by considering an air bubble immersed in water. In addition, the exact value of the resonance peak according to Eq. (25) is also depicted in Fig. 14. Inspection of Fig. 14 reveals that the approximate expression for $Y_{apy-\mathrm{peak}}$ is accurate enough to calculate the resonance peak.

V. CONCLUSION

In this paper, the theory for acoustic radiation force exerted by SSAWs is extended to a compressible sphere in inviscid fluids, based on which the resonance of a gas bubble is further analyzed to provide better estimations for both the resonance point and peak. The derivation starts from the scattered theory and is accomplished using the near-field derivation approach. Our extended theory is examined by recovering the formulas derived in PTWs and PSWs, when Rayleigh angles are equal to 0° and 90°, respectively. Numerical calculations are carried out to illustrate the Rayleigh angle effects on the radiation force.

In the direction normal to the piezoelectric substrate, the radiation force caused by the SSAW shows great dependence on the Rayleigh angle. More specifically, with the increase of the Rayleigh angle, the acoustic radiation force exhibits an overall decreasing trend, and reverses its direction when the Rayleigh angle approaches 90°. In the direction parallel to the piezoelectric substrate, the Rayleigh angle plays a dominant role in both the magnitude and direction of the radiation force, providing an approach to actively tune the equilibrium positions (i.e., pressure nodes or antinodes) for particle positioning. When a bubble is illustrated by SSAWs, both the resonance point and peak exhibit great dependence on the Rayleigh angle. We provide simple and accurate expressions to estimate the two values. These have great potential in SSAWs-based bubble manipulations.

ACKNOWLEDGMENT

This work is supported by the National Natural Science Foundation of China (Grant No. 51575441).

APPENDIX: SPECIAL FUNCTIONS USED IN THE DERIVATION

In the derivation of Eq. (4), we use the following identity,

$$e^{i\mathbf{k}\cdot\mathbf{r}} = \sum_{n=0}^{\infty} i^n j_n(kr)(2n+1) \times \left[P_n(\cos(\theta_k)) P_n(\cos(\theta_r)) + 2\sum_{m=1}^{n} \frac{(n-m)!}{(n+m)!} P_n^m(\cos(\theta_k)) P_n^m(\cos(\theta_r)) e^{im(\varphi_r-\varphi_k)} \right]. \tag{A1}$$

In the derivations of Eq. (17) and Eq. (25), the following equations are used,

$$\int_0^{2\pi} \cos n\theta \cos m\theta \cos\theta d\theta = \begin{cases} \pi & (n+m=1) \\ \frac{\pi}{2} & (n-m=\pm 1, \\ 0 & n\neq 0, m\neq 0) \\ & \text{otherwise} \end{cases}, \tag{A2a}$$

$$\int_0^{2\pi} \sin n\theta \sin m\theta \cos\theta d\theta = \begin{cases} \frac{\pi}{2} & (n-m=\pm 1, \\ 0 & n\neq 0, m\neq 0) \\ & \text{otherwise} \end{cases}, \tag{A2b}$$

$$\int_0^{2\pi} \cos n\theta \sin m\theta \sin\theta d\theta = \begin{cases} 0 & (n=1, m=0) \\ \pi & (n=0, m=1) \\ \frac{-\pi}{2} & (n-m=1, m\neq 0) \\ \frac{\pi}{2} & (m-n=1, n\neq 0) \\ 0 & \text{otherwise} \end{cases}, \tag{A2c}$$

$$\int_0^{2\pi} \cos n\theta \cos m\theta \sin\theta d\theta = 0. \tag{A2d}$$

In Eq. (A2), $F_n(x_f)$ could represent either $j_n(x_f)$ or $n_n(x_f)$,

$$x_f F_n'(x_f) = nF_n(x_f) - x_f F_{n+1}(x_f), \tag{A3a}$$

$$x_f F_{n+1}'(x_f) = x_f F_n(x_f) - (n+2)F_{n+1}(x_f). \tag{A3b}$$

The relation between $j_n(x_f)$ and $n_n(x_f)$ can be written as

$$j_{n+1}(x_f)n_n(x_f) - j_n(x_f)n_{n+1}(x_f) = 1/x_f^2. \tag{A4}$$

[1] J. Wu, Z. He, Q. Chen, and J. M. Lin, Biochemical analysis on microfluidic chips, TrAC, Trends Anal. Chem. **80**, 213 (2016).

[2] J. W. Choi, K. W. Oh, J. H. Thomas, W. R. Heineman, H. B. Halsall, J. H. Nevin, A. J. Helmicki, H. T. Henderson, and C. H. Ahn, An integrated microfluidic biochemical detection system for protein analysis with magnetic bead-based sampling capabilities, Lab Chip **2**, 27 (2002).

[3] Q. Feng, J. Sun, and X. Jiang, Microfluidics-mediated assembly of functional nanoparticles for cancer-related pharmaceutical applications, Nanoscale **8**, 12430 (2016).

[4] J. Friend and L. Y. Yeo, Microscale acoustofluidics: Microfluidics driven via acoustics and ultrasonics, Rev. Mod. Phys. **83**, 647 (2011).

[5] K. Kurihara, H. Ohkawa, Y. Iwasaki, O. Niwa, T. Tobita, and K. Suzuki, Fiber-optic conical microsensors for surface plasmon resonance using chemically etched single-mode fiber, Analytica Chimica Acta **523**, 165 (2004).

[6] H. Zhu, X. Lin, Y. Su, H. Dong, and J. Wu, Screen-printed microfluidic dielectrophoresis chip for cell separation, Biosens. Bioelectron. **63**, 371 (2015).

[7] F. Petersson, L. Åberg, A.-M. Swärd-Nilsson, and T. Laurell, Free flow acoustophoresis: microfluidic-based mode of particle and cell separation, Anal. Chem. **79**, 5117 (2007).

[8] A. Lenshof, C. Magnusson, and T. Laurell, Acoustofluidics 8: applications of acoustophoresis in continuous flow microsystems, Lab Chip **12**, 1210 (2012).

[9] D. L. Miller, N. B. Smith, M. R. Bailey, G. J. Czarnota, K. Hynynen, I. R. S. Makin, and American Institute of Ultrasound in Medicine Bioeffects Committee, Overview of therapeutic ultrasound applications and safety considerations, J. Ultrasound Med. **31**, 623 (2012).

[10] P. Augustsson, C. Magnusson, M. Nordin, H. Lilja, and T. Laurell, Microfluidic, label-free enrichment of prostate cancer cells in blood based on acoustophoresis, Anal. Chem. **84**, 7954 (2012).

[11] D. Magaña-Ortíz, N. Coconi-Linares, E. Ortiz-Vazquez, F. Fernández, A. M. Loske, and M. A. Gómez-Lim, A novel and highly efficient method for genetic transformation of fungi employing shock waves, Fungal Genet. Biol. **56**, 9 (2013).

[12] P. B. Muller and H. Bruus, Theoretical study of time-dependent, ultrasound-induced acoustic streaming in microchannels, Phys. Rev. E Stat Nonlin Soft Matter Phys. **92**, 063018 (2015).

[13] R. Klíma and V. A. Petržílka, On the radiation pressure of electromagnetic wave packets in nondispersive fluid dielectrics, Ann. Phys. **92**, 395 (1975).

[14] Louis V. King and F. R. S., On the acoustic radiation pressure on spheres, Proc. R. Soc. London **147**, 212 (1934).
[15] K. Yosioka and Y. Kawasima, Acoustic radiation pressure on a compressible sphere, Acta Acust. Acust. **5**, 167 (1955).
[16] L. P. Gor'Kov, On the forces acting on a small particle in an acoustical field in an ideal fluid, Soviet Physics Doklady **6**, 773 (1962).
[17] T. Hasegawa and K. Yosioka, Acoustic-radiation force on a solid elastic sphere, J. Acoust. Soc. Am. **46**, 1139 (1969).
[18] T. Hasegawa, Comparison of two solutions for acoustic radiation pressure on a sphere, J. Acoust. Soc. Am. **61**, 1445 (1977).
[19] T. Hasegawa, Acoustic radiation force on a sphere in a quasistationary wave field-theory, J. Acoust. Soc. Am. **65**, 32 (1979).
[20] T. Hasegawa and Y. Watanabe, Acoustic radiation pressure on an absorbing sphere, J. Acoust. Soc. Am. **63**, 1733 (1978).
[21] Wei Wei, D. B. Thiessen, and P. L. Marston, Acoustic radiation force on a compressible cylinder in a standing wave, J. Acoust. Soc. Am. **116**, 201 (2004).
[22] S. F. Morse, D. B. Thiessen, and P. L. Marston, Capillary bridge modes driven with modulated ultrasonic radiation pressure, Phys. Fluids **8**, 3 (1996).
[23] M. J. Marr-Lyon, D. B. Thiessen, and P. L. Marston, Stabilization of a cylindrical capillary bridge far beyond the Rayleigh-plateau limit using acoustic radiation pressure and active feedback, J. Fluid Mech. **351**, 345 (1997).
[24] M. J. Marr-Lyon, D. B. Thiessen, and P. L. Marston, Passive Stabilization of Capillary Bridges in Air with Acoustic Radiation Pressure, Phys. Rev. Lett. **86**, 2293 (2001).
[25] P. L. Marston and D. B. Thiessen, Manipulation of fluid objects with acoustic radiation pressure, Ann. N.Y. Acad. Sci. **1027**, 414 (2004).
[26] S. D. Danilov and M. A. Mironov, Mean force on a small sphere in a sound field in a viscous fluid, J. Acoust. Soc. Am. **107**, 143 (2000).
[27] A. A. Doinikov, Acoustic radiation force on a spherical particle in a viscous heat-conducting fluid. ii. Force on a rigid sphere, J. Acoust. Soc. Am. **101**, 722 (1997).
[28] A. A. Doinikov, Acoustic radiation pressure on a rigid sphere in a viscous fluid, in *Proceedings of the Royal Society of London A: Mathematical, Physical and Engineering Sciences* (The Royal Society, London, 1994), Vol. 447, pp. 447–466.
[29] M. Settnes and H. Bruus, Forces acting on a small particle in an acoustical field in a viscous fluid, Phys. Rev. E **85**, 016327 (2012).
[30] J. T. Karlsen and H. Bruus, Forces acting on a small particle in an acoustical field in a thermoviscous fluid, Phys. Rev. E **92**, 043010 (2015).
[31] S. Annamalai, S. Balachandar, and M. K. Parmar, Mean force on a finite-sized spherical particle due to an acoustic field in a viscous compressible medium, Phys. Rev. E **89**, 053008 (2014).
[32] F. G. Mitri and Z. E. A. Fellah, Axial acoustic radiation force of progressive cylindrical diverging waves on a rigid and a soft cylinder immersed in an ideal compressible fluid, Ultrasonics **51**, 523 (2011).
[33] M. Barmatz and P. Collas, Acoustic radiation potential on a sphere in plane, cylindrical, and spherical standing wave fields, J. Acoust. Soc. Am. **77**, 928 (1985).
[34] T. Hasegawa, M. Ochi, and K. Matsuzawa, Acoustic radiation force on a solid elastic sphere in a spherical wave field, J. Acoust. Soc. Am. **69**, 937 (1981).
[35] P. L. Marston, Axial radiation force of a Bessel beam on a sphere and direction reversal of the force, J. Acoust. Soc. Am. **120**, 3518 (2006).
[36] R. Wu, X. Liu, and X. Gong, Axial acoustic radiation force on a sphere in Gaussian field, in *Recent Developments in Nonlinear Acoustics: International Symposium on Nonlinear Acoustics Including the International Sonic Boom Forum* (AIP, Melville, 2015), pp. 301–311.
[37] F. G. Mitri, Axial acoustic radiation force on rigid oblate and prolate spheroids in bessel vortex beams of progressive, standing and quasi-standing waves, Ultrasonics **74**, 62 (2017).
[38] J. Shi, D. Ahmed, X. Mao, S. C. Lin, A. Lawit, and T. J. Huang, Acoustic tweezers: patterning cells and microparticles using standing surface acoustic waves (SSAW), Lab Chip **9**, 2890 (2009).
[39] S. Liang and W. Chaohui, Revised model for the radiation force exerted by standing surface acoustic waves on a rigid cylinder, Phys. Rev. E **97**, 033103 (2018).
[40] S. Liang and W. Chaohui, Acoustic radiation force on a compressible cylinder in the standing surface acoustic wave (SSAW), J. Appl. Phys. **123**, 044504 (2018).
[41] T. Zhu, R. Cheng, S. A. Lee, E. Rajaraman, M. A. Eiteman, T. D. Querec, E. R. Unger, and L. Mao, Continuous-flow ferrohydrodynamic sorting of particles and cells in microfluidic devices, in *Microfluidics and Nanofluidics* (Springer, New York, 2012), pp. 1–10.
[42] X. Ding, S.-C. Steven Lin, M. I. Lapsley, S. Li, X. Guo, C. Y. Chan, I.-K. Chiang, L. Wang, J. P. McCoy, and T. J. Huang, Standing surface acoustic wave (SSAW)-based multichannel cell sorting, Lab Chip **12**, 4228 (2012).
[43] L. Ren, Y. Chen, P. Li, Z. Mao, P.-H. Huang, J. Rufo, F. Guo, L. Wang, J. P. McCoy, S. J. Levine *et al.*, A high-throughput acoustic cell sorter, Lab Chip **15**, 3870 (2015).
[44] G. Destgeer, Byung Hang Ha, J. Park, J. H. Jung, A. Alazzam, and H. J. Sung, Microchannel anechoic corner for size-selective separation and medium exchange via traveling surface acoustic waves, Anal. Chem. **87**, 4627 (2015).
[45] G. Destgeer, K. H. Lee, J. H. Jung, A. Alazzam, and H. J. Sung, Continuous separation of particles in a PDMS microfluidic channel via traveling surface acoustic waves (TSAW), Lab Chip **13**, 4210 (2013).
[46] J. Shi, H. Huang, Z. Stratton, Y. Huang, and T. J. Huang, Continuous particle separation in a microfluidic channel via standing surface acoustic waves (SSAW), Lab Chip **9**, 3354 (2009).
[47] Z. Tengfei, W. Chaohui, N. Dong, J. Weitao, S. Yongsheng, Y. Lei, C. Bangdao, L. Hongzhong, and D. Yucheng, Exploitation of surface acoustic waves to drive nanoparticle concentration within an electrification-dependent droplet, RSC Advances **4**, 46502 (2014).
[48] X. Ding, J. Shi, S.-C. Steven Lin, S. Yazdi, B. Kiraly, and T. J. Huang, Tunable patterning of microparticles and cells using standing surface acoustic waves, Lab Chip **12**, 2491 (2012).
[49] D. J. Collins, B. Morahan, J. Garcia-Bustos, C. Doerig, M. Plebanski, and A. Neild, Two-dimensional single-cell patterning with one cell per well driven by surface acoustic waves, Nat. Commun. **6**, 8686 (2015).

[50] S. Li, X. Ding, F. Guo, Y. Chen, M. I. Lapsley, S.-C. Steven Lin, L. Wang, J. P. McCoy, C. E. Cameron, and T. J. Huang, An on-chip, multichannel droplet sorter using standing surface acoustic waves, Anal. Chem. **85**, 5468 (2013).

[51] J. H. Jung, G. Destgeer, B. Ha, J. Park, and H. J. Sung, On-demand droplet splitting using surface acoustic waves, Lab Chip **16**, 3235 (2016).

[52] J. K. R. Weber, C. A. Rey, J. Neuefeind, and C. J. Benmore, Acoustic levitator for structure measurements on low temperature liquid droplets, Rev. Sci. Instrum. **80**, 083904 (2009).

[53] A. Ye, C. K. Sanders, and B. L. Marrone, Separation of Escherichia colibacteria from peripheral blood mononuclear cells using standing surface acoustic waves, Anal. Chem. **85**, 9126 (2013).

[54] J. Nam, Y. Lee, and S. Shin, Size-dependent microparticles separation through standing surface acoustic waves, Microfluid. Nanofluid. **11**, 317 (2011).

[55] J. Nam, H. Lim, C. Kim, J. Y. Kang, and S. Shin, Density-dependent separation of encapsulated cells in a microfluidic channel by using a standing surface acoustic wave, Biomicrofluidics **6**, 24120 (2012).

[56] Y. Chen, A. A. Nawaz, Y. Zhao, P. H. Huang, J. P. Mccoy, S. J. Levine, L. Wang, and T. J. Huang, Standing surface acoustic wave (SSAW)-based microfluidic cytometer, Lab Chip **14**, 916 (2014).

[57] K. Lee, H. Shao, R. Weissleder, and H. Lee, Acoustic purification of extracellular microvesicles, Acs Nano **9**, 2321 (2015).

[58] Y. Chen, S. Li, Y. Gu, P. Li, X. Ding, L. Wang, J. P. McCoy, S. J. Levine, and T. J. Huang, Continuous enrichment of low-abundance cell samples using standing surface acoustic waves (SSAW), Lab Chip **14**, 924 (2014).

[59] S. Li, X. Ding, Z. Mao, Y. Chen, N. Nama, G. Feng, L. Peng, W. Lin, C. E. Cameron, and T. J. Huang, Standing surface acoustic wave (SSAW)-based cell washing, Lab Chip **15**, 331 (2015).

[60] A. Eller, Force on a bubble in a standing acoustic wave, J. Acoust. Soc. Am. **43**, 170 (1968).

[61] S. Annamalai and S. Balachandar, Mean force on a finite-sized rigid particle, droplet, or bubble in a viscous compressible medium, Phys. Fluids **27**, 103304 (2015).

[62] C. P. Lee and T. G. Wang, Acoustic radiation force on a bubble, J. Acoust. Soc. Am. **93**, 1637 (1998).

[63] X. Ding, P. Li, S.-C. Steven Lin, Z. S. Stratton, N. Nama, F. Guo, D. Slotcavage, X. Mao, J. Shi, F. Costanzo *et al.*, Surface acoustic wave microfluidics, Lab Chip **13**, 3626 (2013).

[64] A. A. Doinikov, Translational motion of a spherical bubble in an acoustic standing wave of high intensity, Phys. Fluids **14**, 1420 (2002).

[65] D. Ahmed, X. Mao, J. Shi, B. K. Juluri, and T. J. Huang, A millisecond micromixer via single-bubble-based acoustic streaming, Lab Chip **9**, 2738 (2009).

[66] X. Ding, Z. Peng, S.-C. Steven Lin, M. Geri, S. Li, P. Li, Y. Chen, M. Dao, S. Suresh, and T. J. Huang, Cell separation using tilted-angle standing surface acoustic waves, Proc. Natl. Acad. Sci. **111**, 12992 (2014).